Modeling and simulation results on high sensitivity scattered gamma-ray emission imaging

C. Driol [a,*], M.K. Nguyen [b], T.T. Truong [a]

[a] *LPTM, CNRS UMR 8089, Université de Cergy-Pontoise, 2 rue Adolphe Chauvin, 95302 Cergy-Pontoise Cedex, France*
[b] *ETIS, CNRS UMR 8051, ENSEA, Université de Cergy-Pontoise, 6 avenue du Ponceau, 95014 Cergy-Pontoise Cedex, France*

ARTICLE INFO

ABSTRACT

A new modality in gamma-ray emission imaging, based on the use of scattered radiation detected with an uncollimated gamma camera, is put forward. Recently, we have shown that scattered radiation by Compton effect registered on a collimated gamma camera can be in principle used to reconstruct an object in three dimensions. To improve drastically the sensitivity of this process, we propose that data acquisition should be performed without mechanical collimation. As a first step, image formation in two dimensions is derived and validated by Monte Carlo simulations. Then, numerical reconstructions are presented to support the feasibility and attractiveness of this new concept.

1. Introduction

Scattered radiation imaging is a promising modality in gamma-ray emission imaging with potential applications in many fields such as bio-medical imaging, gamma-ray astronomy, non-destructive industrial testing, environmental survey and control, etc. Conventionally, three-dimensional reconstruction techniques use non-scattered (or primary) radiation and consider scattered radiation as noise which should be removed as much as possible. However, since the 1950s, Compton scattered radiation and its possible usages for tomography as well as for three-dimensional imaging have experienced a growing interest [1,3,5,6]. Different proposals have been put forward to implement this idea, among which, for example, Compton tomography [11] and Compton camera imaging [12].

Recently, we have proposed to collect information carried by scattered radiation registered by a collimated gamma camera for imaging purposes [9]. In this new imaging principle, it is shown that a series of images generated by scattered radiation at different scattering energies forms a complete set of data for three-dimensional object reconstruction [8,10]. Since each scattering energy is connected to a single scattering angle by the Compton relation, the Compton scattering angle plays effectively the role of the spatial angle of rotation of a gamma camera in conventional tomography procedures. Hence, data acquisition can be carried out advantageously by a camera operating in a fixed position. We have established that three-dimensional reconstruction of an object is possible since an analytic inversion formula exists, at least when attenuation is

---

* Corresponding author. Tel.: +33 1 34 25 75 07.
 E-mail address: clemence.driol@u-cergy.fr (C. Driol).

neglected and the electronic density of the scattering medium roughly constant. However, the presence of the collimator reduces enormously the number of detected photons since a great number of them are absorbed by the collimator. Thus, to increase the image sensitivity, we propose to work without collimation. Our operating modality is nevertheless different from that of a Compton camera since radiation scattering takes place throughout the object and no coincidence detection is necessary as in the Compton camera. In this situation, a detection site will register many more contributions arriving from all possible directions from the upper half-space of the detector [4]. To focus first on the essentials of image formation and convey the key aspects of this new modality, we choose in this paper to present the discussion in two dimensions for which the computations are less involved and more manageable.

This paper is organized as follows. Section 2 describes the successive steps of image formation with and without collimation. In Section 3, we present details of the calculation of the theoretical expressions of the point spread function (PSF) in these two cases. To compare the sensitivity between these two modalities and test the accuracy of our image formation model, we compute numerically, in Section 4, the PSF and compare it to the ones obtained by Monte Carlo simulations. Finally in Section 5, we show numerical reconstruction results which illustrate the possible implementation of this new imaging principle. Conclusion and perspectives appear in Section 6.

2. Image formation in two dimensions

As pointed out earlier, the working of this imaging modality will be considered in two dimensions to avoid unnecessary computational complications and stress the key ideas. Here, we think of a two-dimensional space as a slice of a three-dimensional medium. Therefore, physical quantities used, such as linear attenuation coefficient, scattering cross section, electron density, etc. are those of three-dimensional space restricted to an infinitely thin layer.

The object is to compute the photon flux density reaching a detection site from a radiating object, described by an activity density function $f(\mathbf{S})$ (number of photons emitted per unit time per unit object volume, assumed to be isotropic).

Let

- $\mathbf{S} = (x_S, y_S)$ be a point source of activity density $f(\mathbf{S})$,
- $\mathbf{M} = (x_M, y_M)$, a scattering site inside the object surrounding medium,
- $n_e(\mathbf{M})$, the electron density at site $\mathbf{M}$,
- $\mathbf{D} = (x_D, y_D)$, a detection site on a linear detector which collects scattered photons at scattering energy E_ω (see Eq. (1)).

The energy E_ω of a scattered photon is related to its scattering angle ω by the Compton relation

$$E_\omega = E_0 \frac{1}{1 + (E_0/mc^2)(1 - \cos\omega)}, \tag{1}$$

where E_0 is the emitted photon energy and mc^2 the rest energy of the electron.

From Fig. 1, one can see that the photon flux density reaching a site $\mathbf{M}$ is the number of photons emitted into the angular fan $d\Omega$ per unit length and per unit time

$$\frac{f(\mathbf{S})\,dS_S}{2\pi} \phi(\mathbf{S} \to \mathbf{M}) \frac{1}{\sigma}, \tag{2}$$

where

$$\phi(\mathbf{S} \to \mathbf{M}) = d\Omega = 2\arctan\left(\frac{\sigma}{2|SM|}\right), \tag{3}$$

- dS_S is the area element around $\mathbf{S}$,
- $|SM|$ is the distance between sites $\mathbf{S}$ and $\mathbf{M}$,
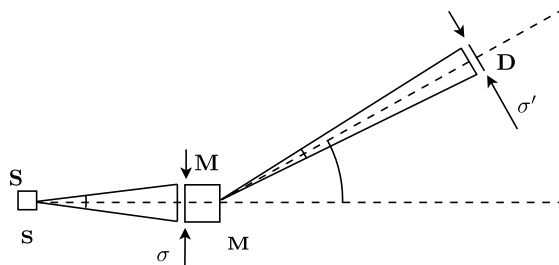- σ is the width of a scattering medium square.

Fig. 1. Geometry of Compton scattering: source site $\mathbf{S}$, scattering site $\mathbf{M}$ of width σ, detection site $\mathbf{D}$ of width σ'.

The fraction of photons scattered in the direction making an angle ω with the incident direction depends on the Compton differential cross section $\sigma_C(\omega)$, on the number of electrons around site **M** and on the angular fan $d\Omega'$ under which is viewed the detecting element of size σ'. This cross section gives the probability for a photon to be scattered in a direction making an angle ω with the incident direction and it is written as

$$\sigma_C(\omega) = \frac{1}{2}\pi r_e^2 \, P(\omega), \tag{4}$$

where $P(\omega)$ is the Klein–Nishina scattering probability [5], r_e is the classical radius of the electron and the $1/2$ factor indicates that the photon has the same probability to go on one or the other branch of the two-dimensional cone of opening angle ω.

The scattered photon flux density received at the detection site **D** is now given by

$$d\Phi(\mathbf{D}, \omega|\mathbf{S}, \mathbf{M}) = \frac{f(\mathbf{S}) \, dS_S}{2\pi} \phi(\mathbf{S} \to \mathbf{M}) \frac{1}{\sigma} \, \sigma_C(\omega) \, n_e(\mathbf{M}) \, dS_{\mathbf{M}} \frac{1'}{\sigma} \phi(\mathbf{M} \to \mathbf{D}), \tag{5}$$

where $\phi(\mathbf{M} \to \mathbf{D})$ is defined as in Eq. (3) and σ replaced by σ'.

The total photon flux density at a site **D** is the integral over all source sites and all scattering sites such that the scattering angle is ω. This constraint is expressed by a δ-function as follows:

$$\Phi(\mathbf{D}, \omega) = \int \int d\Phi(\mathbf{D}, \omega|\mathbf{S}, \mathbf{M})\delta(\widehat{SMD} - (\pi - \omega)), \tag{6}$$

where $\widehat{SMD}$ is the angle at vertex **M** of the triangle SMD (see Fig. 2).

3. Computation of the image of a point source

The PSF is by definition the image of a single point source at site $\mathbf{S}_0$ and of intensity f_0. Eq. (6) can be rewritten in terms of PSF as follows:

$$g(\mathbf{D}, \omega) = \int dS_S f(\mathbf{S}) \text{PSF}(\mathbf{D}, \omega|\mathbf{S}), \tag{7}$$

where $g(\mathbf{D}, \omega)$ is the number of photons received on a unit area detector pixel at site **D** and at energy E_ω, given by Eq. (1).

An explicit expression of the PSF can be obtained if only single scattering events are considered (they turn out to be the dominant ones as confirmed by Monte Carlo simulations, see Fig. (6)) and if uniform electron density n_e is assumed. The value of the PSF for a point source at site $\mathbf{S}_0$ at detection site **D** and with scattering angle ω has the following expression:

$$\text{PSF}(\mathbf{D}, \omega) = \frac{f_0}{2\pi} n_e \sigma_C(\omega) \int \phi(\mathbf{S}_0 \to \mathbf{M}) \, \phi_N(\mathbf{M} \to \mathbf{D}) \, dS_{\mathbf{M}}, \tag{8}$$

where $\phi_N(\mathbf{M} \to \mathbf{D})$ is the angular fan of photons emitted by the secondary source **M** and detected by a pixel at **D**. It is given by Eq. (9). The scattering sites $\mathbf{M}_1$ and $\mathbf{M}_2$ due to point source $\mathbf{S}_0$ are located on two circular arcs subtending an angle $(\pi - \omega)$ (Eq. (6)).
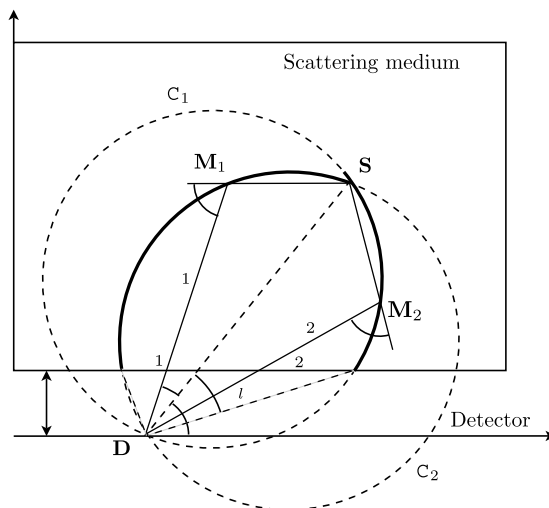

Fig. 2. Scattering sites contributing to detection site D without collimator (bold circular arcs).

In the integrand of Eq. (8), three terms depend on **M**:

- $\phi(\mathbf{S} \to \mathbf{M})$ is given by Eq. (3), where $f(\mathbf{S})\,dS_S = f_0 \delta(\mathbf{S} - \mathbf{S}_0)\,dS_S$,
- The second factor in the integrand depends on the detector pixel, that is, its spacial resolution $\Delta\sigma'(d\omega)$ at its energy resolution dE (which is related to $d\omega$, the acceptance angle around a value ω of the scattering angle)

$$\phi_N(\mathbf{M} \to \mathbf{D}) = 2 \arctan\left(\frac{\Delta\sigma'(d\omega)\cos\theta}{2|MD|}\right), \tag{9}$$

where $\Delta\sigma'(d\omega)\cos\theta$ is an effective area facing arriving photons on the detection pixel at energy resolution dE (or $d\omega$) under an angle θ, as shown in Fig. 3,
- dS_M is the scattering site area.

To compute these three terms, we use polar coordinates (r, γ) centered at **D**, for which one has $\mathbf{S} = (d, \alpha)$ with $|DS| = d$, $\mathbf{M} = (r, \gamma)$ with $|MD| = r$ and $\overrightarrow{DM} \cdot \overrightarrow{DS} = rd\cos\gamma$.

The circular arcs are then given by the equations

$$r_1 = d\frac{\sin(\omega - \gamma_1)}{\sin\omega} \quad \text{and} \quad r_2 = d\frac{\sin(\omega + \gamma_2)}{\sin\omega}. \tag{10}$$

Then

- to compute $\phi(\mathbf{S} \to \mathbf{M})$, we need the distance $|SM|$. It can be extracted from a simple identity in the triangle DSM

$$|SM| = d\frac{\sin\gamma}{\sin\omega}, \tag{11}$$

- to compute $\phi_N(\mathbf{M} \to \mathbf{D})$, we need the product $\Delta\sigma'(d\omega) \cdot \cos\theta$. It can easily be obtained in polar coordinates as

$$\Delta\sigma'(d\omega)\cos\theta = \frac{d}{\sin(\omega)} \cdot \frac{2\sin(d\omega)\sin(\omega - \gamma)\sin(\alpha - \gamma)}{\cos(\omega) - \cos(2(\alpha - \gamma))} \cdot \sin(\alpha - \gamma), \tag{12}$$

- to compute the scattering site area dS_M, we use its expression $\lambda \cdot \varepsilon(\gamma)$, as shown in Fig. 3. λ is an infinitesimally small arc length given by

$$\lambda = \sqrt{dr^2 + r^2\,d\gamma^2} = \frac{d}{\sin\omega}d\gamma. \tag{13}$$

The distance $\varepsilon(\gamma)$ between the two circular arcs is computed by locating the intersections of a straight line passing through the center of the median circle and the two circle arcs, if the pixel detector width σ' is not equal to zero (see Fig. 3). Its expression is not simple and will be evaluated numerically.

Finally, the PSF is given by the sum of the integration on γ over the two arcs of circle

$$\begin{aligned} \text{PSF}(\mathbf{D}, \omega|\mathbf{S}) = f_0 n_e r_e^2 P(\omega)\frac{d}{(\sigma\sin\omega)} \sum_{2\,\text{Arcs}} \\ \times \int_0^{\gamma_l(\omega)} \arctan\left(\frac{\sigma\sin(\omega)}{2\,d\sin(\gamma)}\right)\arctan\left(\frac{\sin(\alpha - \gamma)2\sin(d\omega)}{\cos(\omega) - \cos(2(\alpha - \gamma))}\right)\varepsilon(\gamma)\,d\gamma. \end{aligned} \tag{14}$$
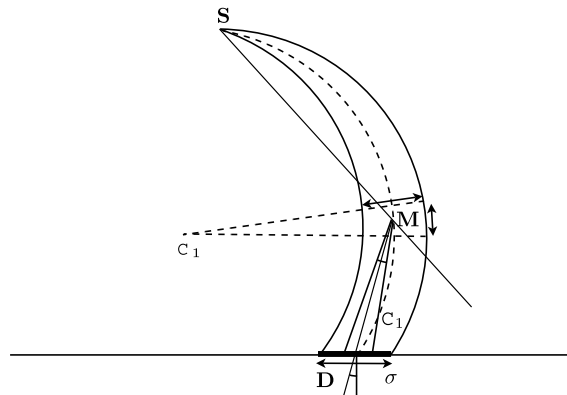

Fig. 3. Details of the curves used in the calculation in overblown proportions.

The integration is to be carried out over points inside the scattering medium. Therefore, when the medium is of finite extent, the limits of integration $\gamma_l(\omega)$, which correspond to the intersections of the arcs of circle with the scattering medium, should be calculated beforehand (see Fig. 2).

Now, if the collimator is mounted on the detector, only one scattering site **M**, located on the perpendicular to the detector at site **D**, will contribute to the detection site **D**, (see Fig. 4). Thus, the integration on γ is restricted by a delta function which picks out only a small interval $[-\varsigma_{col}, \varsigma_{col}]$ focused on the corresponding value of γ:

$$\gamma_{col} = \left(\frac{\pi}{2} - \alpha\right). \tag{15}$$

The resulting PSF expression for a collimated detector is

$$\begin{aligned}\text{PSF}_{col}(\mathbf{D}, \omega|\mathbf{S}) = & K(\omega) \int_{-\varsigma_{col}}^{\varsigma_{col}} \arctan\left(\frac{\sigma \sin(\omega)}{2\,d\sin(\gamma)}\right) \\ & \times \arctan\left(\frac{\sin(\alpha - \gamma)2\sin(d\omega)}{\cos(\omega) - \cos(2(\alpha - \gamma))}\right)\varepsilon(\gamma)\delta(\gamma - \gamma_{col})\,d\gamma,\end{aligned} \tag{16}$$

where ς_{col} is the acceptance angle of the collimator.

4. Comparison between PSF modeling and Monte Carlo simulations

In this section, we compute numerically the theoretical PSF function, obtained in the previous section, as a function of detector position for a given value of the scattering angle ω and simulate the PSF by Monte Carlo techniques under the same conditions. Comparison of the results will help to confirm the validity of our approach.

The scattering medium is represented by a rectangular medium of dimensions 30 cm × 15 cm, which is at a distance of 1 cm above a linear detector. Since biological tissues have an electronic structure close to that of water, we shall take $n_e = 3.34 \times 10^{23}$ electrons/cm^3. A point source is placed in the scattering medium at 6 cm above the detector. The radio pharmaceutical used in this simulation is medical Technecium 99, which emits photons with energy 140.1 keV. The activity density of the source is about 27×10^{-3} Ci/cm^3, with an acquisition time per image of one second. The linear detector is formed by 256 pixels of length 0.11 cm and is placed along the 0x-axis. The acceptance angle of the collimator ς_{col} is 0.1 rad.

Monte Carlo techniques are nowadays widely used in medical imaging to accurately simulate physical processes undergone by photons from emission to detection (medium absorption, scattering of different types) [13–15]. They have reached a high degree of sophistication and reliability, as they are now tailored to work under specific conditions [7]. The package GATE–GEANT4 dedicated to emission tomography is certainly a well-known example [2]. Thus, we turn to Monte Carlo simulations to generate the PSF of our imaging system using scattered radiation, first to compare with the one given by theoretical considerations and second to estimate the contributions of higher order scattering events.

We chose to write our own code to focus on the effect of attenuation along the photon propagation path in matter. The collimator is characterized by an acceptance cone, but the detection in the detector is not simulated here. We assume that the medium attenuation is due simultaneously to photoelectric absorption and Compton scattering at energies from 90 to 140 keV (see Table 1) [16]. The running time with MatLab is about a few days. Moreover two types of simulations are carried
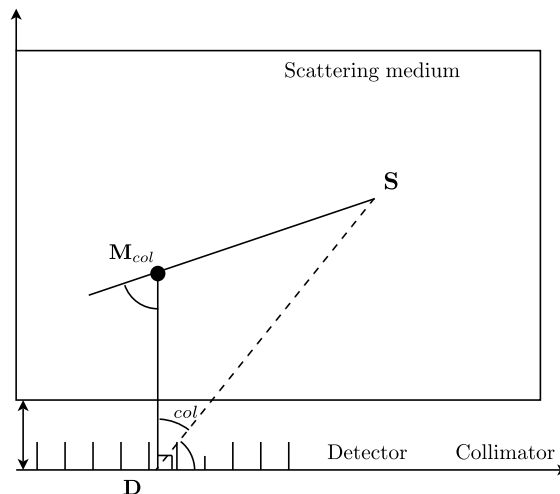

Fig. 4. Single scattering site (bold spot) contributing to detection site D with collimator.

out respectively with single scattering and with multiple scattering. The discrepancy in the results of these two cases would yield an estimate of the accuracy of the hypothesis of single scattering process in the theoretical approach.

For this purpose, we introduce an attenuation coefficient in Eq. (14):

$$
\begin{aligned}
\text{PSF} = & K(\omega) \sum_{2 \text{ Arcs}} \int_{\mathbf{M} \in \text{ medium}} e^{-\mu_0 |SM|} e^{-\mu_\omega |ML|} \\
& \times \arctan\left(\frac{\sigma \sin(\omega)}{2 \, d \sin(\gamma)}\right) \arctan\left(\frac{\sin(\alpha - \gamma) 2 \sin(d\omega)}{\cos(\omega) - \cos(2(\alpha - \gamma))}\right) de(\gamma) \, d\gamma,
\end{aligned}
\tag{17}
$$

where μ_0 and μ_ω are the linear attenuation coefficients at energies E_0 and E_ω and

$$
|ML| = \frac{d}{\sin(\omega)} \sin(\omega - \gamma) - \frac{l}{\sin(\alpha - \gamma)}
$$

is the distance from site **M** to site **L**, intersection of the line *MD* with the horizontal line $y = l$, representing the medium lower limit (see Fig. 2). The integration is then performed numerically.

Fig. 5 shows results of first-order Monte Carlo simulations. We represent the number of photons registered by the detector as a function of the scattering angle (degrees) and the detector position (cm). The relative error for the PSF without col-

Table 1
Linear attenuation coefficients for water [16]

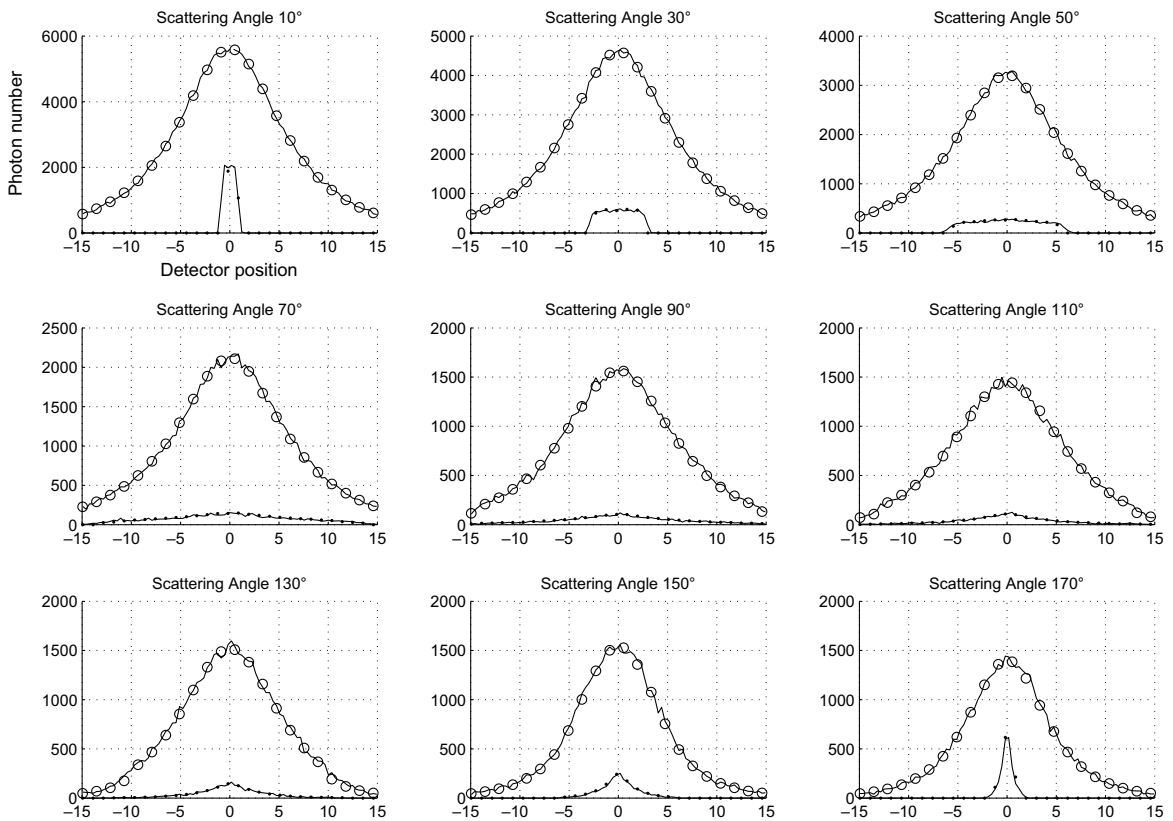| Energy (keV)	Attenuation coefficient (cm^{-1})	Scattering coefficient (cm^{-1})	Absorption coefficient (cm^{-1})
140	0.1538	0.1511	0.0028
120	0.1614	0.1574	0.0040
100	0.1706	0.1646	0.0060
80	0.1833	0.1728	0.0105

Fig. 5. Comparison of PSF profiles (Monte Carlo simulation (line) and forward model (points)) for a camera with (white points) and without (black points) collimator. The number of detected events is plotted against the detector pixel linear position on both sides of the point source position.
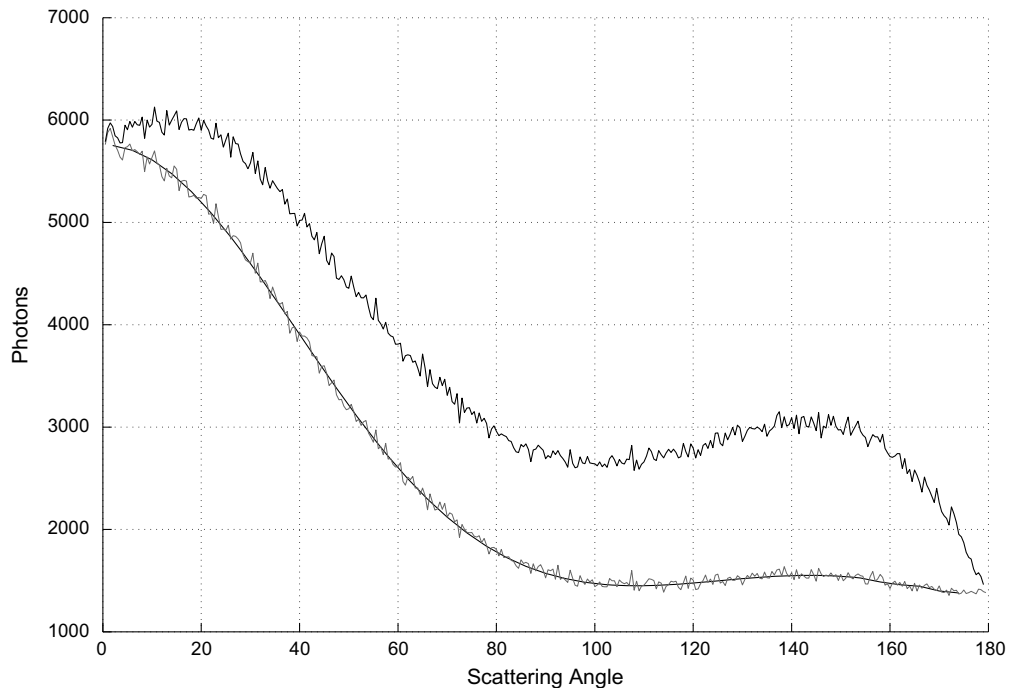
Fig. 6. Comparison of first-order (lower lines) and multi-order (upper line) scattering Monte Carlo simulations.

limator between the first-order (single scattering) Monte Carlo simulation and our forward model is about 4%. For the PSF with collimator, this error is 12%.

At a fixed scattering angle ω, the PSF curve as a function of the detector position with collimator has a 'mesa' shape while the PSF curve without collimator has a wide Lorentzian shape. On the whole, the detector without collimator collects about 12 times more photons than with collimator.

In Fig. 6, we show results of Monte Carlo simulations to compare the contributions of first-order scattering with higher order scattering contributions. We observe that multiple scattering contributions increase as one goes from low scattering angles to high scattering angles. But the dominance of single scattering events remains clear.

5. Numerical reconstruction results

As an illustration on the possibility of using a uncollimated camera in this new modality, we carried out two numerical reconstructions. First we present the reconstruction of the single point source from Monte Carlo simulated data. Next we show the reconstruction of the Shepp–Logan medical phantom from data computed with our model.

5.1. Numerical point source reconstruction

The scattering medium is discretized with 41 points in $0x$-axis direction and with 22 points in $0y$-axis direction. The detector size is reduced to 86 pixels, each one distant from the next by 0.35 cm. We keep the same pixel size as in Section 4. The detector records 44 images of photon energies from 139 to 90.5 keV. The single point source is centered at 6 cm above the detector line.

We construct the two weight matrices of the medium by calculating from our models (with and without collimator), for each point of the mesh, the PSF at different scattering angles. The size of the two weight matrices is 3784×902. This large number of equations compared to the number of unknowns reduces the conditional number (3×10^3 for camera with collimator and 7×10^4 for camera without collimator).

We use the Monte Carlo simulated gamma-ray data detected by a camera with or without collimator for the reconstruction. The reconstruction is carried out by using the conjugated gradient method with positivity constraint.

In the two cases, the source activity is faithfully reconstructed (about 10^9 photons per second). For a camera with collimator, the Conjugated Gradient method gives an acceptable reconstruction with 100 iterations, and must be regularized by limiting the number of iterations. Fig. 7 corresponds to 500 iterations.

When the collimator is removed, the reconstruction gives correct results even for a large iteration number. Fig. 8 corresponds to 500 iterations.
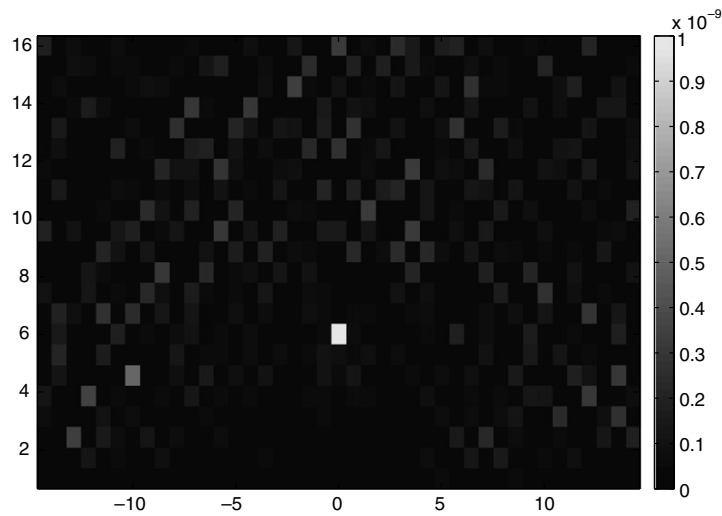
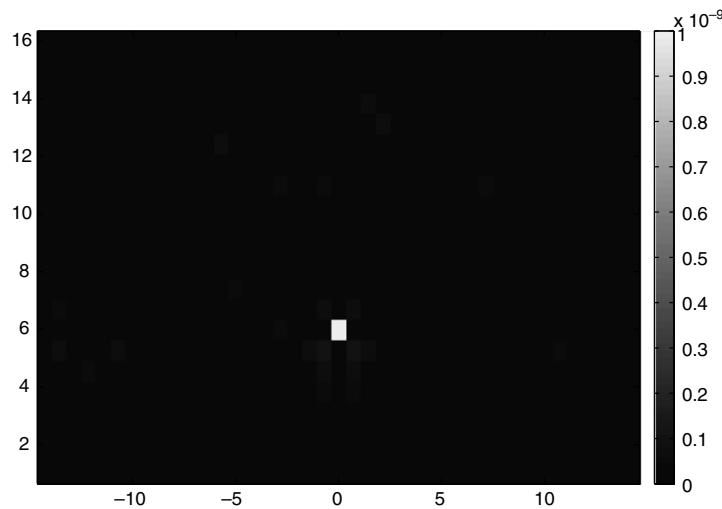**Fig. 7.** Point source reconstruction from Monte Carlo simulated images with a camera with collimator.

Fig. 8. Point source reconstruction from Monte Carlo simulated images with a camera without collimator.

5.2. Numerical image reconstruction results

The object is an 2D original Shepp–Logan medical phantom, representing the activity density of the object (see Fig. 9). It is placed at the center of the scattering medium and at a unit distance above the detector. A line detector of 55 pixels of 1 unit length, placed on the axis $y = 0$, is simulated. We consider that the scattering medium has the same attenuation characteristics as water. It consists of a discretized square of 55×55 elements of unit area.

A series of 55 views of the object corresponding to 55 different scattering angles $(12^{\circ} < \omega < 132^{\circ})$ have been simulated. Images without collimator are on the average 23 times more sensitive than those with collimator. We construct the 3025×3025 weight matrix by computing, for each mesh point source, the PSF at the different scattering angles for each site on the detector. The reconstruction is carried out by inverting the weight matrix using the singular value decomposition method, which is less time consuming compared to the conjugate gradient method.

Figs. 10 and 11 show the reconstruction results with and without collimator. One observes a better agreement with the original object when the collimator is removed. In this case, the relative error is $4.8 \times 10^{-5}\%$ instead of 8% when the collimator is mounted.
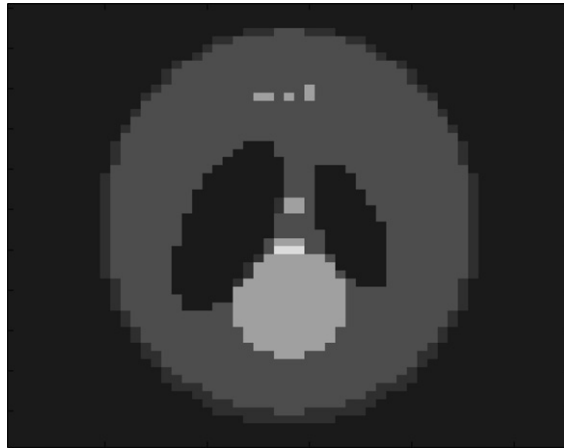
Fig. 9. Original Shepp–Logan phantom.

Fig. 10. Shepp–Logan phantom reconstruction with collimator.

Fig. 11. Shepp–Logan phantom reconstruction without collimator.

6. Conclusion

In this work, we have used extensive numerical calculations and Monte Carlo simulations to validate a new concept in gamma-ray emission imaging without collimation. Such a methodological approach is the best way to demonstrate the feasibility of the idea before working with real data. The essence of this new concept of high sensitivity imaging system, which operates a *fixed* uncollimated camera, consists of collecting *all* relevant first-order scattered rays, instead of rejecting them as done in current imaging systems, and use them for object reconstruction purposes. Work aiming at extending image formation modeling and simulations of related scattered radiation in three dimensions is in progress.

References

[1] B. Bridge, F. Harirchian, D.C. Imrie, Y. Mehrabi, A.R. Meragi, Experiments in Compton scatter imaging of materials with wide-ranging densities using a low-activity gamma source, NDT&E Int. 20 (1987) 339–346.
[2] I. Buvat, D. Lazaro, Monte Carlo simulations in emission tomography and GATE: an overview, Nucl. Instr. Math. A 569 (2006) 323–329.
[3] R.L. Clarke, E.N.C. Milne, G. Van Dyk, The use of Compton scattered gamma rays for tomography, Invest. Radiol. 11 (1976) 225–235.
[4] C. Driol, M.K. Nguyen, T.T. Truong, On high sensitivity emission imaging by scattered gamma radiation, in: Proceedings of the IEEE Engineering in Medicine and Biology Conference 29, Lyon, France, 2007.
[5] B.L. Evans, J.B. Martin, L.W. Burggaf, M.C. Roggemann, Nondestructive inspection using Compton scatter tomography, Proc. IEEE Nucl. Sci. Symp. 45(3) (1997) 386–390.
[6] E.M.A. Hussein, Compton scatter imaging systems, in: D.L. Wise (Ed.), Bioinstrumentation: Research, Developments and Applications, Butterworth, London, 1990, pp. 1053–1086.
[7] C. Morel, Monte Carlo simulation in nuclear medicine, Méd. Nucl. 31 (2007) 160–164.
[8] M.K. Nguyen, T.T. Truong, On an integral transform and its inverse in nuclear imaging, Inverse Probl. Eng. 18 (2002) 265–277.
[9] M.K. Nguyen, T.T. Truong, J.L. Delarbre, N. Kitanine, Three-dimensional Object Reconstruction from Compton Scattered Gamma Ray Data, Computer Vision and Mathematical Methods in Medical and Biomedical Image Analysis, Springer, Berlin, 2004. pp. 24–34..
[10] M.K. Nguyen, T.T. Truong, H.D. Bui, J.L. Delarbre, A novel inverse problem in gamma-ray emission imaging, Inverse Probl. Eng. 12 (2004) 225–246.
[11] S.J. Norton, Compton scattering tomography, J. Appl. Phys. 76 (1994) 2007–2015.
[12] M. Singh, An electronically collimated gamma camera for single photon emission computed tomography. Part 1: Theoretical considerations and design criteria, Med. Phys. 10 (1983) 421–427.
[13] H. Zaidi, Relevance of accurate Monte Carlo modeling in nuclear imaging, Med. Phys. 26 (1999) 574–608.
[14] H. Zaidi, Addendum to relevance of accurate Monte Carlo modeling in nuclear imaging, Med. Phys. 27 (2000) 816–817.
[15] H. Zaidi, Monte Carlo modeling in nuclear medicine imaging, in: H. Zaidi (Ed.), Quantitative Analysis in Nuclear Medicine Imaging, Springer, New York, 2006, pp. 358–390.
[16] http://physics.nist.gov/PhysRefData/XrayMassCoef.